Sea level trends across the Bahamas constrain peak Last Interglacial ice melt

Blake Dyer[a,b], Jacqueline Austermann[a], William J. D'Andrea[a], Roger C. Creel[a], Michael R. Sandstrom[a], Miranda Cashman[a], Alessio Rovere[a,c], and Maureen E. Raymo[a]

[a]Lamont-Doherty Earth Observatory, Columbia University, 61 Route 9W, Palisades, NY, 10964, USA; [b]School of Earth and Ocean Sciences, University of Victoria, Victoria, BC, Canada; [c]MARUM – Center for Marine Environmental Sciences, University of Bremen, DE

This manuscript was compiled on May 25, 2021

During the last interglacial period (LIG), global mean sea level was higher than present, likely driven by greater high-latitude insolation. Past sea level estimates require elevation measurements and age determination of marine sediments that formed at or near sea level, and those elevations must be corrected for glacial isostatic adjustment (GIA). However, this GIA correction is subject to uncertainties in the GIA model inputs, namely Earth's rheology and past ice history, which reduces precision and accuracy in estimates of past global mean sea level (GMSL). To better constrain the GIA process, we compare new and existing last interglacial sea-level data across the Bahamian archipelago to a suite of 576 GIA model predictions. We calculated weights for each GIA model based on how well the model fits spatial trends in the regional sea-level data and then used the weighted GIA corrections to revise estimates of GMSL during the last interglacial. During the LIG, we find a 95% probability that global sea level peaked at least 1.2 m higher than today and it is very unlikely (5% probability) to have exceeded 5.3 m. Estimates increase by up to 30% (decrease by up to 20%) for portions of melt that originate from the Greenland Ice Sheet (West Antarctic Ice Sheet). Altogether, this work suggests that last interglacial global mean sea level may be lower than previously assumed.

last interglacial sea level | glacial isostatic adjustment | The Bahamas

The geologic record suggests that peak global mean sea level was +6-9 m higher than today during the Eemian, or last interglacial (LIG; ∼130–116 ka ago; (1–3)). However, global mean temperature was only slightly warmer than pre-industrial values, likely due to greater high latitude summer insolation at that time (+1-2°C; (4)). If such modest warming can cause a +6-9 m rise in sea level, then the sea level response to ongoing and future warming will likely be drastic (5, 6). While +6 meters of global mean sea level (GMSL) rise could be explained by thermal expansion of the oceans and the near complete melting of the Greenland ice sheet (4), significant melting of ice on Antarctica must occur to reach +9 m (7). This significant uncertainty demonstrates that improving LIG GMSL estimates is needed to better understand past, and hopefully future, ice sheet responses to warming.

Past GMSL estimates are derived by measuring the elevation and age of marine sediments that formed at or near sea level on passive margins, and correcting those elevations for glacial isostatic adjustment (GIA; the elastic and viscoelastic response of the solid Earth, its gravity field, and rotation axis, to the redistribution of ice and water; (8–11)). On glacial-interglacial timescales, topographic change due to GIA depends on the history of ice distribution on land (12) and the magnitude and rate of Earth deformation under that load (i.e. its rheology; (9, 13)). Changes in topography, and hence local sea level, also can be caused by cooling of the lithosphere and mantle convection (dynamic topography; (14–18)), tectonics, or deformation associated with sediment redistribution.

For the LIG, uncertain knowledge of Earth's internal viscosity, past ice sheet history, and dynamic topography hinder the determination of a precise and accurate estimate of GMSL (18–20). Specifically, while the magnitude of postglacial rebound in the vicinity of former ice sheets has been used to constrain the viscosity of Earth's interior (13, 21, 22), large uncertainties persist concerning both the most appropriate 1D and the global 3D viscosity structure of the mantle. When reconstructing ice history, it is often assumed that the penultimate glacial maximum (MIS 6) ice sheet history (e.g. location and mass of ice sheet loading) was very similar or identical to that of the last glacial maximum (MIS 2). However, even small differences in the ice sheet history between MIS 2 and MIS 6 could change GMSL inferred from tropical regions by several meters (19, 20). Lastly, models and observations of dynamic topography (DT) suggest that paleo sea level indicators in a single location could uplift or subside by several meters since the LIG, even on passive margins (18, 23).

The Bahamian archipelago is a tectonically stable region that has three important features that make it ideal for reducing GIA uncertainty and improving estimates of past GMSL. First, GIA models predict that this region, on the peripheral forebulge of the Laurentide Ice Sheet (LIS), should have large lateral variations in relative sea level ((2); Fig.1), and the magnitude and shape of these variations depend on mantle viscosity and past ice history. Observations of contemporane-

Significance Statement

The seas are rising as the planet warms, and reconstructions of past sea level provide critical insight into the sensitivity of ice sheets to warmer temperatures. Past sea level is reconstructed from the geologic record by measuring the elevations of fossilized marine sediments and coral reefs. However, the elevations of these features also record local uplift or subsidence due to the growth and decay of ice sheets since the time of deposition. We compare new observations of paleo sea level across the Bahamian archipelago to a range of Earth deformation models to revise estimates of last interglacial global mean sea level. Our results suggest that polar ice sheets may be less sensitive to high latitude warming than previously thought.

B.D., J.A., W.J.D., A.R. and M.E.R. designed research; all authors participated in field work; J.A. generated GIA models; B.D. wrote the code for and did the analysis for the model-data comparisons and Bayesian inversion; B.D. wrote the paper and drafted figures with input from all other authors.

We have no competing interests to declare.

[2]To whom correspondence should be addressed. E-mail: blakedyer@uvic.ca

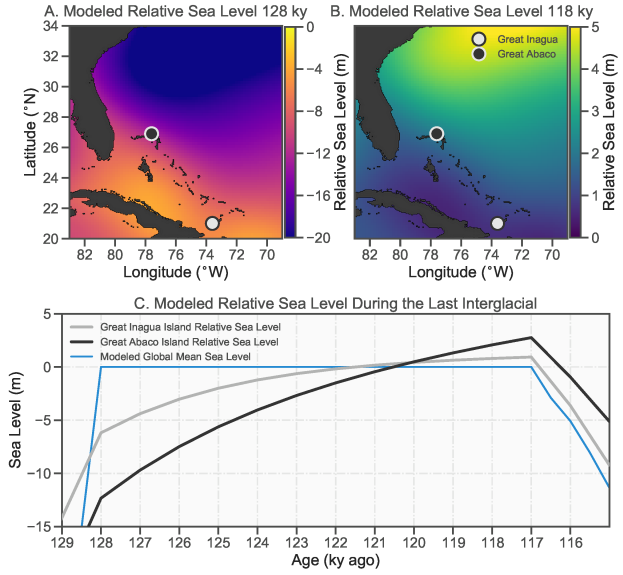

Fig. 1. A. Modeled sea level at the start of the last interglacial relative to today assuming no change in global mean sea level during the LIG. This number is equal to the elevation relative to sea level today that one would find a sediment that records sea level from the start of the LIG if global mean sea level did not exceed present values. B. Modeled sea level at the end of the last interglacial relative to today assuming no change in global mean sea level during the LIG. C. Change in modeled local sea level for Great Inagua and Great Abaco. The GIA model used here has a lower mantle viscosity of 5×10^{21} Pa·s, upper mantle viscosity of 0.5×10^{21} Pa·s, and a lithosphere thickness of 96 km; the MIS6 ice sheet size and geometry is equal to the last glacial maximum. See Methods for more details.

ous paleo sea-level can therefore directly constrain these GIA model choices. Second, subsurface core data (24) can be used to constrain long-term subsidence and regional deformation that may have occurred due to dynamic topography or other slow processes such as tectonics, karst isostasy, sediment loading, or the cooling of the lithosphere. Third, the sediments of the Bahamas are excellent archives of past sea level (25–29). In this paper, we compare new and existing observations of paleo sea level across the archipelago to a range of GIA model predictions to identify those GIA model inputs that are consistent with lateral variations in the sea level observations. 576 unique GIA models are combined based on how well the model fits lateral variations in regional sea-level data, and this weighted GIA correction is used to revise estimates of GMSL during the last interglacial.

Results and Discussion

Geology of the Bahamian archipelago. The sedimentary rocks that make up the islands of the Bahamian archipelago are primarily narrow aeolian or storm ridges that accumulated above sea level and broad limestone flats that accumulated underwater during times in the past when sea level was higher than today. The elevations of these two types of sediments provide upper and lower limits, respectively, for sea level in the past (25, 30–34).

The narrow ridges run along the windward (north-east) shorelines of most islands and are the highest landforms in the archipelago, commonly reaching elevations of +20-30 meters. Occasional gaps in these shore-parallel ridges contain slightly lower elevation U or V shaped ridges that point and extend in the landward direction (32, 33, 35). The limestone flats are typically on the western side of islands at elevations of less than 7 meters above modern sea level. Vertical exposures of these limestone flats along coastal cliffs or in sinkholes exhibit unambiguous marine features, such as fossil corals and traces of other marine organisms.

These exposures of LIG marine sediments can typically be described as shallowing-upward parasequences (25) where, over several meters, a decrease is observed in the apparent water depth in which the sediments were accumulating. The lowermost sediments in a parasequence often contain corals or burrow-filled carbonate sands and muds with marine fossils. Moving upward, mud and fine sand is rarer, replaced by coarser carbonate sands that are typically cross-stratified, which signifies transport by currents and waves. These cross-stratified sand units transition upwards into well-sorted sands with nearly parallel mm-thin beds that dip towards the paleo-coastline (27, 36, 37). This transition sometimes is marked by tabular intraclasts with worn or abraded surfaces. Such intraclasts are found along beaches in the Bahamas today, which also consist of nearly parallel-bedded and well-sorted sands. In most locations, the top of the parasequence contains cross-stratified sand with abundant root casts and fossilized land snails, an indication of aeolian or terrestrial deposition. The contact between these uppermost aeolian units and the lower lying beach sediments is a snap shot of past sea level. More specifically, this contact marks the the landward swash limit of constructive waves, or the elevation of the ancient ordinary berm (38).

Modern observations suggest that the shallowing component of the shallowing-upwards parasequence is likely a record of rapid accumulation of sediment, rather than a change in sea level. These deposits typically form along the margins of islands where the rate of sedimentation outpaces the generation of accommodation space (by subsidence, for instance). As sediment fills the available space, there is a coinciding decrease in water depth. For example, many Holocene beaches in the Bahamas are currently prograding seaward even though there has been sea level rise in the region throughout the Holocene (39) (presumably due to glacial isostatic adjustment). A stratigraphic section through a modern beach would reveal sediments that record an upwards decrease in water depth. Based on the above observations, we investigated LIG progradational deposits across the Bahamas and use the highest elevation of the contact between aeolian facies and underlying beach facies as indication of local peak LIG sea level. Because the region can be expected to subside by up to 10 meters due to GIA throughout an interglacial, we expect that the highest beach facies on each island will have formed towards the end of the LIG and that the age of these peak local sea level deposits is similar across the archipelago.

Peak LIG sea level across the archipelago. An obvious multi-meter decrease in the maximum elevation of LIG beach facies is observed across the archipelago from north to south (Figs. 2 and S1). For example, on the island of Eleuthera (northern Bahamas), the highest beach facies are found at Whale Point at an elevation of 6.7 m. In contrast, on Great Inagua (southern Bahamas) the highest elevation marine sediments are part of an aeolian capped shallowing upwards parasequence where the beach to aeolian transition is only 2.3 m above mean tide level (at Matthew Town). In other locations surveyed, the LIG peak

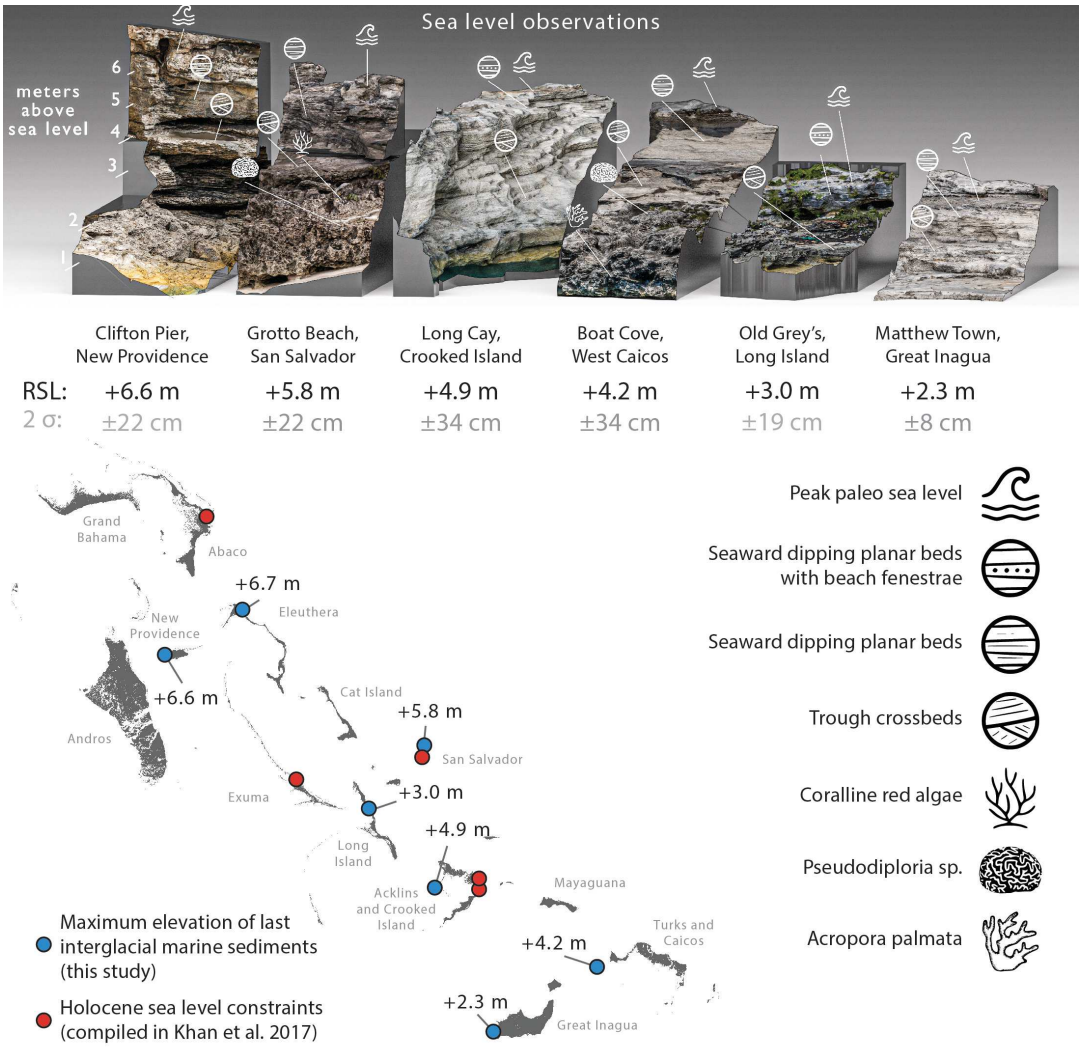

Fig. 2. The highest surveyed elevations of the contact between LIG beach and aeolian sediments from seven surveyed islands are annotated on a map of the Bahamas. Orthographic renders of six outcrops illustrate the typical shallowing-upwards parasequences of the Bahamas.

local sea level changes gradually between islands, generally decreasing towards the south and southwest (Fig. 2).

On a single island, such as San Salvador, beach sediments within LIG parasequences record sea level at various elevations. At the Cockburn Town reef outcrop, the maximum elevation of beach sands is 3.7 ±0.1 meters above mean tide level. However, 10 km to the south at Grotto Beach, there are beach sediments as high as 5.8±0.22 m. Both outcrops have corals in the basal units that grew during the LIG (27, 36). The difference in the elevation of these beach facies indicates that the sea level of San Salvador Island changed by several meters during the LIG. Local sea level is determined primarily by glacial isostatic adjustment and changes in global mean sea level. Each location records sea level at the moment when the accommodation space filled with sediment and transitioned to a terrestrial environment.

To determine peak LIG sea level on islands that were not directly surveyed in the field, peak LIG sea level was estimated from satellite-derived maps of elevation. The islands comprise terrestrial and marine landforms that were classified into three categories: Holocene beaches and marshes, aeolian dune ridges, and marine limestone flats (see Methods). The elevation of marine limestone flats decreases across the archipelago to the south and west, generally matching the pattern observed in outcrop (Fig. S1). These elevations provide a lower bound for peak LIG local sea level (that is, these satellite-derived estimates are treated as marine-limiting).

Glacial isostatic adjustment in the Bahamas. The islands of the Bahamas experience significant sea level rise during interglacial periods due to GIA (Fig. 1; (40–43)). During glacial periods, the mass of the Laurentide ice sheet depresses the underlying North American crust and forces mantle material to flow away from that depression. This flow to the ice periphery causes uplift in many regions, including the Bahamas. During an interglacial, the formerly glaciated regions rebound and the displaced mantle material migrates northward causing subsidence of the peripheral high. Thus, at the start of an interglacial, the Bahamas region is elevated relative to today and sea level indicators on Great Inagua from this time (at 128 ka for instance; Fig. 1) would now be about 6 meters below present-day sea level (assuming that GIA is the only

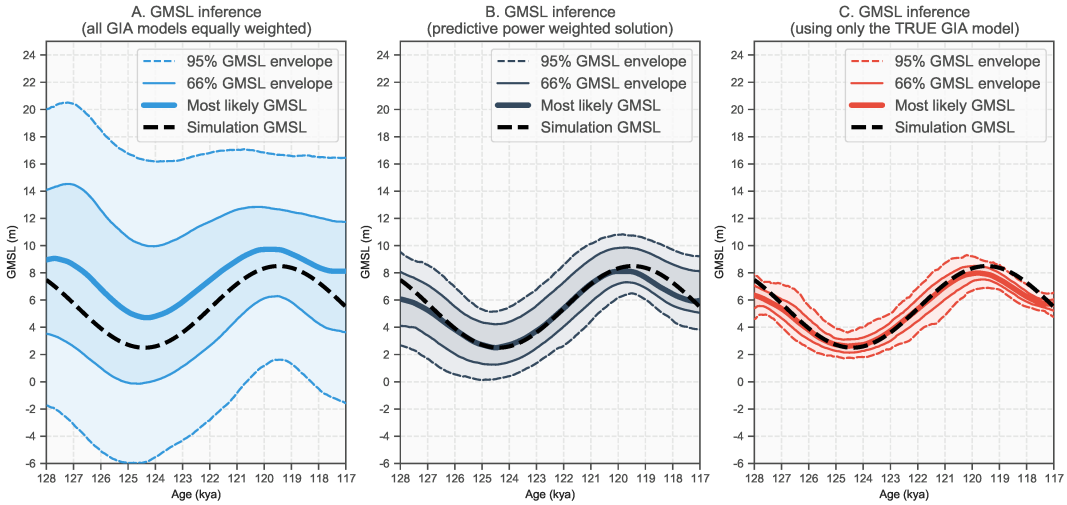

Fig. 3. GMSL inference from the synthetic dataset that differs from the real sea-level data analyzed in this paper only in that the elevations were changed to match a prescribed GMSL curve (shown as dashed black line) and a single GIA model. Panel A shows the estimated GMSL when all 576 GIA models are considered equally probable. Panel B shows the solution where models are weighted by their ability to reproduce the spatial trends across the data (the approach used with the real data in this study). Panel C shows the best solution possible if the true GIA in the region was perfectly known.

factor causing relative sea level change).

Furthermore, the predicted magnitude of GIA is greater in the northern islands than in the southern islands (Fig. 1A). As the archipelago subsides throughout the interglacial (Fig. 1), the magnitude of this subsidence decreases with distance from the former ice sheet (southward). Thus, sediments that recorded sea level at the start of the last interglacial will have subsided more in the north than in the south, and any observed elevation of paleo sea-level from that time will also be lower in the north (Fig 1A). Conversely, sediments (parasequences) that record sea level toward the end of the last interglacial will be higher in the north relative to coincident sediments in the south (Fig 1B). Thus, the spatial pattern of peak local sea level, as inferred from parasequences in progradational LIG sedimentary systems, is a simple test on the relative timing of peak local sea level.

The GIA predicted late LIG relative sea level (RSL) patterns (higher RSL in the north than the south) match the observed peak LIG sea level patterns. Both the field and satellite observations show a clear decrease to the south and west in the maximum elevation of LIG marine sediments (Figs. 2 and S1). The details of the GIA induced paleo sea-level gradient are sensitive to both the viscosity structure of the Earth as well as the size and distribution of the former (MIS 6) North American ice sheet. Uncertainty in these model parameters translates into uncertainty in the inferred paleo GMSL predictions derived from regional data.

Determining the most likely GIA history. We determine the accuracy of individual GIA models by identifying those input parameters (Earth viscosity and ice history) that result in relative sea level predictions that best match the elevation differences of observed sea level across the islands. For example out of a suite of GIA predictions we only retain those that yield RSL predictions late in the LIG that are high in the north and low in the southwest. We quantify how well a specific GIA prediction fits the sea level trends and assign a relative weight to each model. Uncertainties in observed sea level and the formation age of the observations are fully incorporated into these model weights (see Methods). We highlight that this approach does not make any assumptions about GMSL since sea level trends across the archipelago at a given time are independent of the GMSL. Likewise if we were to use only two observations with very different ages (e.g. the beginning and the end of the LIG), the data would put no constraint on the GIA models as the sea level difference could be due to changes in GMSL. The model weights are used to produce a single weighted mean GIA model, which we use to correct our RSL observations.

LIG RSL observations for the region include previously published coral data as well as new island-specific estimates of peak RSL (from both satellite-derived and field surveys). Where absolute ages from corals exist (West Caicos, San Salvador, New Providence and Great Inagua), the ages of corals span the early interglacial through ~119 ky (27, 29, 36, 37, 44). The sands that prograde over these coral outcrops are younger than the corals, and often are the seaward-most strands of prograding beach systems. Invariably, these overlying beach deposits have been interpreted by previous studies as the final phase of the LIG, and the elevations of these features generally support interpretations of a late LIG local sea level high in the region inferred from stranded tidal notches (45, 46). Our observations and interpretations of the geology agree with these previous studies (see Dataset S1); however, we will argue that most of the increase in local sea level during the LIG results from GIA subsidence.

Bayesian inversion and a synthetic test. Bayesian gaussian process regression was used to estimate GMSL during the LIG from a set of new and existing Bahamian sea level observations. Each sea level observation was corrected for the indicative water depth range of the observation, the long term subsidence of the archipelago, and for GIA using a weighted combination of 576 distinct GIA models. Our fully Bayesian gaussian process framework provides the statistical tools to incorporate data with very different age uncertainties and indicative water

depth ranges to estimate how GMSL (and the uncertainty) changes over time (see Materials and Methods). Long-term subsidence is assumed to be the same across the archipelago (2.5 ±1 meters per 125 ky; (24, 47)). Large lateral variations in local sea level that are not caused by GIA are not considered in our current analysis, but new data constraints on long-term subsidence across the archipelago could be incorporated into future inversions.

To determine the efficacy of our inversion approach, we designed a test where we prescribed a *true* GMSL curve ("Simulation GMSL") to generate synthetic observations. We then apply our inversion approach to the synthetic data to infer GMSL, which ideally should reproduce the prescribed *true* GMSL curve. We emphasize that, like with real observations, the statistical model has no inherent knowledge about what the *true* GMSL is. First, we randomly selected one of the 576 GIA models to represent the true GIA model in this test. Next, we generated a synthetic dataset using the real locations, elevation uncertainties, ages, age uncertainties, and the indicative meaning of each type of geologic feature described in this paper. The only difference between the real and the synthetic data is that the elevation of each synthetic sea level observation is obtained by combining the synthetic *true* GMSL and the randomly selected *true* GIA model.

This synthetic dataset was then analyzed in an identical manner to the real dataset. The model weights show that a range of GIA models, including the true one, perform well in fitting the predicted sea level gradients as recorded by our synthetic data (Fig. S2). If we were to assume that all GIA models are equally likely to have generated the synthetic data, the inversion results in a large uncertainty in the inferred GMSL (Fig. 3A). However, when we use the inferred weighting for each GIA model which favors those models that match the spatial RSL trend, we significantly lower the uncertainty of our inferred GMSL and find that the *true* GMSL is within 1σ of the most likely GMSL (Fig. 3B). Even if the *true* GIA correction was known, our inferred GMSL will still not perfectly fit the *true* GMSL given the spatial and temporal distribution of our observations and their associated uncertainties (Fig. 3C). This test demonstrates that the approach used here can reproduce the underlying GMSL signal and that it indeed leads to a more accurate and precise inference compared to simply treating all GIA models equal.

Comparison of Bahamas LIG data and 576 distinct GIA models. We considered a suite of 576 GIA predictions spanning 48 solid Earth configurations, 6 ice histories, and 2 penultimate deglacial onset timings (see Materials and Methods). The magnitude of predicted gradients in RSL across the archipelago are most sensitive to the prescribed ice loading history and deglacial rate (Fig. S3). When the modeled penultimate glacial Laurentide ice sheet is large, i.e. comparable to its MIS 2 size, the expected relative sea level gradient in late last interglacial data (as observed today) is mostly flat. That is, the solid Earth in the Bahamas would be expected to be in a similar state of isostatic disequilbrium during the late last interglacial as it is today. When the Laurentide ice sheet is smaller or when the deglacial onset is earlier, the region will have relaxed to a state quite different than present day, resulting in mostly north-south gradients in relative sea level. Generally, models with slower penultimate deglacial rates have higher relative weights, i.e. produce a better fit to the observed RSL gradients (the right 2 columns of Fig. S3). Moreover, with a penultimate glacial ice configuration resembling the last glacial maximum (ICE-6G), no combination of the modeled lithosphere thicknesses or upper or lower mantle viscosity results in RSL gradients that match the observations from the Bahamas (top row of Fig. S3).

The data-model agreement significantly improves when some of the Laurentide ice is redistributed to the Scandinavian ice sheet (smaller Laurentide ice sheet going downwards in Fig. S3). These results are relatively insensitive to changes in lithosphere thickness (even versus odd columns; S3) or upper mantle viscosity (y-axis; S3), within the range of values tested here. Lower mantle viscosity (LMV) is an important input (x-axis; Fig. S3). Models with the smallest Laurentide ice sheet (bottom row of Fig. S3) are more consistent with the observations when LMV is in the lower end of the tested range (LMV of 5–10×10^{21} Pa·s). However, models with the intermediate-sized Laurentide ice sheet favor the higher end of the tested range (LMV of 10–30×10^{21} Pa·s).

The results above suggest that the Laurentide ice sheet was significantly smaller during the penultimate glacial maximum than during the LGM. Of the 576 GIA simulations, the sum of model weights with an ICE-6G configuration for the penultimate glacial is significantly less than 0.1% (Fig. S3). We find (at a 98% probability) that the Laurentide ice sheet was between 16 and 23 meters of sea level equivalent (SLE) ice volume smaller during the penultimate glacial maximum than during the last glacial maximum. We find almost no probability of a larger (<16 m SLE reduction) or smaller (>23 m SLE reduction) Laurentide ice sheet during the penultimate glacial maximum. Thus, paleo sea-level data from the Bahamas strongly demonstrate that the LIS was smaller during the penultimate glacial maximum, consistent with evidence for either less overall ice volume at the time (as suggested in (20)), or larger ice sheets in Europe and Russia (48–50). While there is evidence that the LIS covered a similar extent to the LGM during penultimate glacial cycle (50), the specific timing and volume of that maximum ice load remains uncertain. Improvements to the specific timing of this LIS ice load history will be critically important for future GIA modeling and sea level reconstruction efforts.

In addition to the large suite of GIA models that assume radial symmetry in viscosity (1D GIA models) we also included 3 model simulations with lateral variations in viscosity (3D GIA models; see Materials and Methods). Our inversion showed that these models did not yield a good fit to the observations, which could be driven by an incorrect viscosity structure or an incorrect ice history. A larger suite of 3D GIA models would be desirable, yet exploring the parameter space systematically is very computationally expensive and beyond the scope of this study. Yet we did use the available 3D GIA simulations to test two first-order questions. First, we investigated whether the gradient that is predicted by the 3D GIA model could be matched by a 1D GIA prediction. We found that in all cases, there were 1D models that fit the 3D GIA gradient across the region (the difference between the 3D GIA model and the most similar 1D GIA model was on average 10 cm). Second, we investigated whether the 3D GIA model could bias our result by repeating the synthetic test using one of the 3D GIA models as true input. We found that the true prediction is always within the 95% GMSL envelope and mostly within the

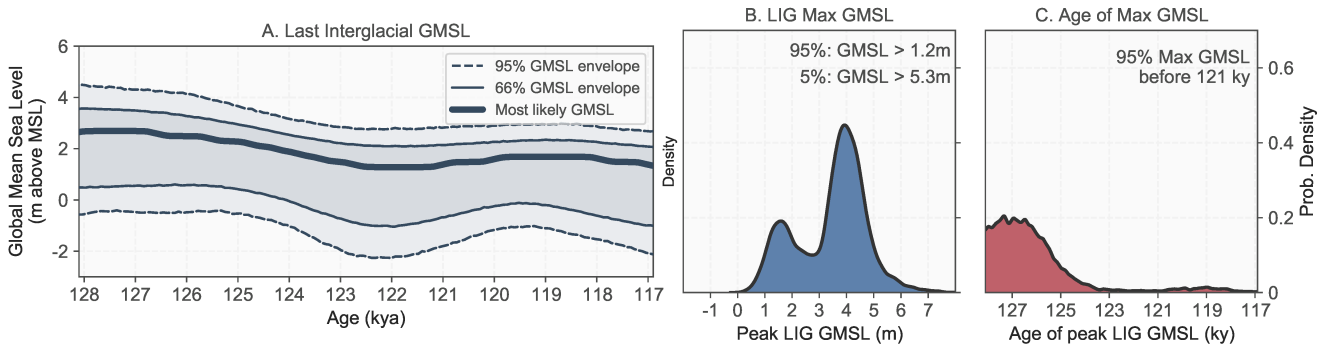

Fig. 4. GMSL estimates for the LIG derived from analysis that includes a probabilistic assessment of 576 GIA models, previously published Bahamian archipelago corals, and the peak local sea level observations reported in this paper. Panel A shows inferred GMSL change throughout the LIG. 68% of the solutions fall within the inner, darker envelope, and 95% of solutions fall within the outer, lighter envelope. Panel B shows the distribution of maximum GMSL (at any point during the LIG), and Panel C shows distribution in time for peak GMSL.

66% envelope of the inferred GMSL. We therefore conclude that 3D viscosity variations are unlikely to largely affect our results but also acknowledge that this result is based on a small set of 3D GIA simulations.

Last interglacial global mean sea level. Gaussian process regression was used to interpolate in time across the set of GIA corrected sea level observations to obtain our estimate of GMSL from this region (see Methods, Fig. 4). Our posterior GMSL curve is lower than previous estimates throughout the LIG, with mean sea level values generally between 0 and 4 m. We find a 95% probability that global mean sea level during the last interglacial period peaked at least 1.2 m higher than today and it is very unlikely (5% probability) to have exceeded 5.3 m (Fig. 4B). It is very likely (95% probability) that this peak GMSL occurs before 121 ka, with the most likely peak occurring at 127 ka (Fig. 4C).

Our analysis supports previous geological arguments for a small oscillation in local Bahamian sea level within the last interglacial. We find it very unlikely that there was an oscillation of GMSL within the LIG that exceeded 1.8 m, and the average inferred oscillation is 0.5 meters. These results are consistent with recently published work arguing for no significant ice sheet regrowth within the LIG (51). On Great Inagua, West Caicos, and San Salvador island, LIG coral reefs are vertically separated into two units by a discontinuous marine-erosion surface that has been interpreted as a rapid GMSL oscillation (27, 37, 52, 53). (29) presented coral ages from the upper and lower units on San Salvador and Great Inagua and argued that the erosion occurred at ∼125 ky and may have lasted up to 1.5 ky (29, 54). RSL estimates for these sites are consistent with this past work (Fig. 5). All sites experience minor erosion followed by relatively stable sea level during the middle of the interglacial, followed by a later rise in local sea level. These two distinct phases of coral growth during the LIG in the Bahamas may reflect an early LIG GMSL peak (Fig. 4) and a regionally amplified (from GIA) late LIG peak (Fig. 5).

Before comparing our GMSL estimates to previously published values we need to consider one additional effect. Our GIA correction does not assume any ice melt during the LIG beyond the present day ice configuration. However, as ice sheets melt they cause an additional distinct spatial pattern of sea level rise due to gravitational and viscoelastic deformation effects (55). For example, if all of the inferred positive GMSL during the LIG is derived from melting the Greenland ice sheet, sea level in the Bahamas will be around 25% lower than the global mean. In other words, an inferred GMSL value of 3 m in the Bahamas that is entirely sourced from the Greenland ice sheet would translate into 4 m of GMSL. Alternatively, if all of the positive GMSL is derived from the West Antarctic Ice Sheet, sea level in the Bahamas will be around 25% higher than the global mean.

High GMSL early in the LIG followed by a more stable climate is generally consistent with reconstructions of LIG atmospheric temperatures in Antarctica and Greenland (56, 57). While the relationship between temperature and ice sheet volume is not straight-forward, coupled regional climate and ice-sheet models of the Greenland ice sheet suggest the maximum contribution to sea level from Greenland occurred at ∼121 ky and ranges from +2.1 m (58) to +5.1 m (59). If the lower end-member is correct, we would expect to see around +1.7 m in the Bahamas, which is in line with our estimates at 121 ky leaving little to no contribution from the Antarctic ice volume beyond its present value. However, if the higher Greenland contribution end-member is correct then larger than present ice sheets must have existed in Antarctica (or elsewhere) at that time. The reconstructions of Greenland contributions to GMSL cited above are not consistent with the peak LIG GMSL at ∼127 ky (Fig. 4C), which suggests that the Antarctic ice sheet was smaller than today at this time. If susceptible sectors of the West Antarctic ice sheets collapsed they would lead to 3.3 m of ice equivalent sea level rise (60), which would be observed as 4.1 m in the Bahamas, an estimate that is in line with the upper end of our inference assuming little to no contribution from the Greenland Ice sheet at this time. This conclusion leads us to hypothesize that the West Antarctic ice sheet collapsed early in the LIG (127-126 ka) but then started to expand while the Greenland ice sheet was shrinking between 126 and 121 ka. Such asynchronicity is supported by the observation that peak temperature anomalies on Antarctica (128.7 ka; (56)) occur earlier than Greenland (126 ka; (57, 59)). Lastly we note that ocean thermal expansion and mountain glaciers contributed to sea level rise during the LIG, but unlikely exceeded 0.4 ± 0.3 m (4) and 0.3±0.1 m (61), respectively.

Our estimates are at odds with the inference by (1) who

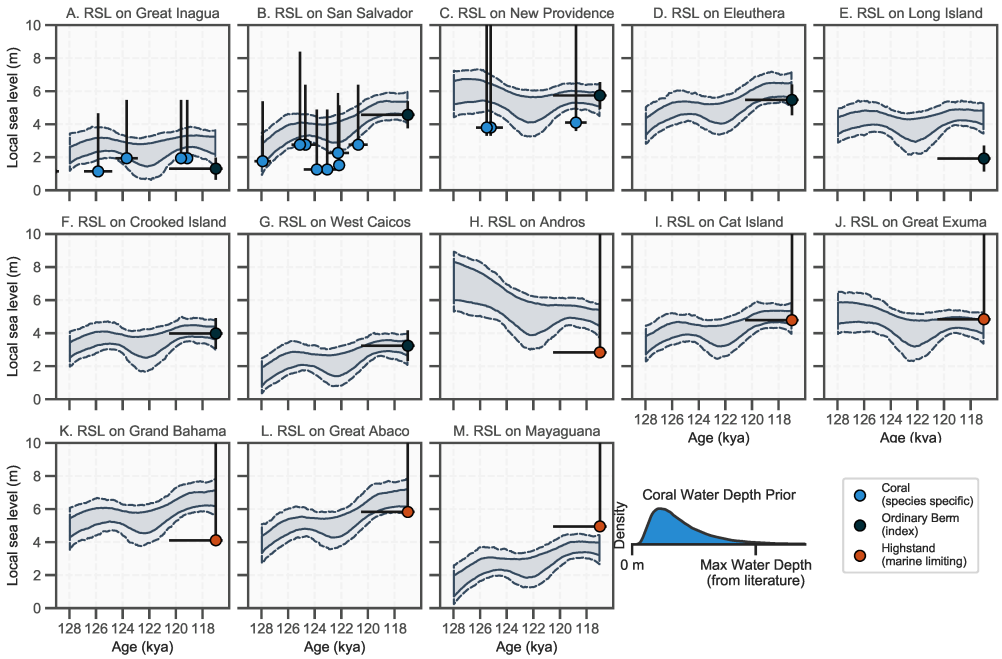

Fig. 5. Inferred site-specific relative sea level. 68% of the solutions fall within the inner, darker envelope, and 95% of solutions fall within the outer, lighter envelope. Coral data is plotted at the elevation of the coral sample today, and the relative sea level uncertainty (the range of possible water depths that the corals lived in) comes from previous work (27, 29, 44, 54, 62). Satellite-derived highstand data are plotted at the observed elevations which are interpreted as the minimum possible relative sea level (marine limiting). Outcrop observations of the boundary between aeolian sand and underlying beach facies are plotted at the observed elevation offset downwards by estimates of the elevation of the landward swash limit of constructive waves (the ordinary berm) (38). Ordinary berm paleo-elevations were estimated using models of site-specific modern day wave run-up and mean high higher water (63).

found that GMSL very likely (95% probability) peaked at least 6.6 m above present-day values. Kopp et al. (2009) included 105 sea level index points and there is no one subgroup of indicators (corals, erosional, facies, isotopic) that if removed lowers their inferred GMSL significantly. We note that their compilation includes several datapoints from the Bahamas and they use a similar longterm subsidence rate for that data to what is used here. The inferred GMSL can nonetheless vary significantly depending on the GIA correction, which we constrain with gradients in LIG relative sea level across the Bahamas. To determine these constraints we have assumed that no other process can explain spatial variations in RSL. While there is good agreement between RSL observations and GIA predictions, which may support a sole GIA origin for the observed lateral gradients, later variability in the longterm subsidence or GIA deformation beyond the range of Earth and ice models tested here can affect our inference. Our estimates are also lower than inferences from coral data from the Seychelles, which indicate that sea level was 7.6 $\pm$ 1.7 m higher than present at 125 ka (3). A higher sea level in the Seychelles could be explained by local uplift, however, there is no evidence to support or repudiate this. Lower GMSL is inferred based on a record of phreatic overgrowths on speleothems in a coastal cave on Mallorca (Spain), but uncertainties associated with the GIA process are on the order of multiple meters at this location making it difficult to draw clear conclusions (64). (65) also argued for lower GMSL that peaked around 4 m during the LIG based on ice-ocean-atmosphere modeling, which is consistent with our findings.

We note that the GIA model weights constrained by Bahamian data are only partly useful for other locations. For example, given real 3D variations in Earth's viscosity, other locations will require GIA models with a different Earth structure. Our inference about the size of the Laurentide ice sheet during MIS 6 will affect the GIA corrections around the globe. However, this inference does not provide great constraints on the extent and ice history of the Fennoscandian ice sheet, which would be needed to improve GIA corrections closer to the Fennoscandian ice sheet.

Conclusions

This work demonstrates that laterally-extensive paleo sea-level data from a region sensitive to GIA model parameters can be used to better constrain those parameters and thus provide more accurate estimates of past GMSL. Our documented southwestward decrease in late LIG sea level indicators across the Bahamas archipelago, apparent in both outcrop and satellite elevation data, can only be reproduced with GIA models that assume a smaller Laurentide ice sheet during the penultimate glacial maximum when compared to the last glacial maximum (a volume reduction of 16–23 meters of sea level equivalence). From an analysis that includes a probabilistic assessment of 576 GIA models, we find that sea level peaked 1.2 – 5.3 m above present levels (95% and 5% probability) and that this peak likely (95% probability) occurred before 121 ka. Our estimate is considerably lower than the currently accepted range of +6.6–9.4 (1, 3), however it is in line with recent climate and sea level modeling (65). We don't find evidence for a significant late rise of global mean sea level associated with a putative rapid collapse of ice sheets after prolonged warming. If true, our results suggest that polar ice sheets may be less

sensitive to high latitude warming than currently believed. Importantly, warming during the LIG was likely insolation driven which may impact each hemisphere at different times. If the melting of northern and southern hemisphere ice sheets was out-of-sync during the LIG, the individual ice sheets may still be very sensitive to local temperature change. Ongoing and future warming is driven primarily by greenhouse gases which should affect both hemispheres more equally.

Materials and Methods

Outcrop surveys . Six islands that span the geographic range of the Bahamas were surveyed to investigate the maximum elevation of local sea level during the LIG. Each outcrop was extensively photographed using a full frame digital camera. The high-resolution 2D photographic data of each outcrop was then transformed into a 3D reconstruction using photogrammetry (from Agisoft Metashape Professional Edition). We measured the latitude, longitude, and elevation of at least five control points at each outcrop with differential GPS. The position of these control points was identified manually on each photograph, and this positional data was used to georeference the 3D outcrop reconstructions. The relative uncertainty within a single outcrop reconstruction (the measured distance between two points or features) is less than a centimeter. The vertical uncertainty of the reconstruction when compared to measurements of local mean sea level or another outcrop is limited by the precision of the differential GPS and includes uncertainty from both measurements. The combined uncertainty is the square root of the sum of the squares of the measured uncertainty from each observation. The uncertainties reported in Fig 2 reflect this combined uncertainty for each outcrop.

We provide a general description of the geologic sites used in this study (Fig. 2), which in part have already been described elsewhere. At each site, we interpret the contact between the beach facies and the overlying aeolinite as the elevation of the landward swash limit of constructive waves (the ordinary berm; (38)).

Clifton Pier, New Providence Island: Exposed along the cliffs of the southwest corner of New Providence Island there are excellent exposures of a last interglacial shallowing-upwards parasequences. The lower 2.5 m contain large (>50 cm) scale trough-cross stratification and intraclast breccia blocks (roughly 50 cm diameter). The intraclasts disappear upwards and the cross bed scale decreases slightly up to about meter 4.5 where the cross stratification transitions into 10-20 cm tabular cross beds. Further upwards, sparse tabular clasts mark the transition from this unit into roughly 2 meters of well-sorted sands with nearly parallel mm-thin beds that dip towards the paleo-coastline. The outcrop is capped by very fine sand that has abundant fossilized root-casts. This unit is described in detail by (66) and many others (25, 31, 39).

Grotto Beach, San Salvador Island: At Grotto Beach, the LIG outcrop extends from the island-ward limit of the modern beach and stretches across the grotto. Immediatly adjacent to the modern beach is a paleo-patch reef containing *Porites astreoides*, *Psuedodiploria sp.* and *Montastrea sp.*. Around 2.5 m above MSL these framework corals are capped by a thin layer (10-20 cm) of corraline red algae (*Neogoniolithon Strictum*). Above, there are 1.5 meters of cross bedded and very poorly sorted (medium to pebble sized) angular carbonate sand. This sand unit is capped by intermittent breccia intra-clasts that transition upwards into well-sorted sands with nearly parallel mm-thin beds that dip towards the paleo-coastline. These nearly parallel-bedded sands persist up to at least 5.8 meters where bedding becomes difficult to discern. The upper-most sediments here have abundant root-casts and are mostly very fine sand (likely aeolian). (36) contains an detailed description and interpretation of this outcrop.

Long Cay, Crooked Island: Roughly 30 km south of Landrail Point along the western margin of Long Cay there is outcrop of a last interglacial progradational strandplain that extends for 4.5 km. The lower 3 m of this sequence contains large-scale (50 cm) cross stratification and abundant *Ophiomorpha* trace fossils (likely shrimp burrows). This lower unit contains occasional thumb-sized coral fragments (*Siderastrea Radians*). There is an irregular and gradual contact between this lower facies and an overlying facies that consists of approximately 2 meters of well-sorted sands with nearly parallel mm-thin beds that dip towards the paleo-coastline. The upper-most part of this unit contains extremely well preserved spherical beach fenestrae (the remnants of air escaping when waves crashed on the ancient beach). Above this fenestrae-bearing beach facies, there are large meter scale fossilized aeolinite dunes. The dune height varies along the 4.5 km coastal outcrop from half a meter to more than 3 meters.

Boat Cove, West Caicos Island: This outcrop is part of an extensive exposure of a LIG reef that spans most of West Caicos island. At this location, the lowermost 2 m is a heavily recrystallized framework of in-situ corals (*Acrapora Palmata* and *Psuedodiploria sp.*). Those corals are capped by 2 m of large-scale (50 cm) cross stratification and abundant *Ophiomorpha* trace fossils (likely shrimp burrows). This cross stratified unit sharply transitions upwards into 1 m of well-sorted sands with nearly parallel mm-thin beds that dip towards the paleo-coastline. The ocean-ward edge of these nearly parallel beds often contain tabular breccia blocks of the same unit (possibly ancient beach rock breccia). This unit is capped with intermittently spaced (10-20 meter) large breccia-filled 'flower-pots'. These features are 1-2 meter diameter round bowl-shaped depressions carved downward into the subplanar beds. Each 'pot' is filled with bright red limestone that contains clasts of recrystallized grey or black limestone. These features may indicate the past location of large plants or palm trees. Reference (37) contains more detailed descriptions of the outcrop on West Caicos.

Old Grey's, Long Island: North east of Anderson's settlement on Long Island there is outcrop of a last interglacial fossil reef that extends for 400 m. On the northern end of this reef, the modern coastline bends westward, and around that bend there is a 3 m high shallowing-upwards parasequence. The lower meter contains large-scale (50 cm) cross stratification. The contact between this lower unit and the overlying unit is difficult to pinpoint. The overlying unit contains well-sorted sands with nearly parallel mm-thin beds that dip towards the paleo-coastline, and the upper-most beds in this unit contain well preserved spherical beach fenestrae.

Matthew Town, Great Inagua Island: In central Matthew Town, the coastal outcrop consists of a last interglacial shallowing-upwards parasequence. The lowermost meter contains abundant large-scale (50 cm) cross stratification and *Ophiomorpha* trace fossils. There is an irregular contact between this cross bedded facies and the overlying facies that consists of well-sorted sands that are arranged in nearly parallel mm-thin beds that dip towards the paleo-coastline. The top of this well-sorted unit contains a 5-8 cm thick deposit with pervasive and irregular cm-scale macro-porosity. This porous unit has been interpreted as a wrack-line or plant accumulation layer at the contact between beach and dunes (67). The upper-most rocks in this location contain very fine sand, and are full of fossilized root-casts.

Quantifying mean sea level: To compare one outcrop to another, or to compare an outcrop to digital elevation maps, we developed a mean sea level reference frame for the surveyed islands (Fig S4). There is a long term tidal and elevation dataset available from Settlement Point on Grand Bahama Island (68). However, sea level relative to the reference ellipsoid measured by GPS (WGS84) varies by 10s of meters across the archipelago. Therefore, we deployed tide gauges in each field area to measure water levels over several days to a week. The water level records were clipped to include roughly the same number of high and low tide events, and mean water level was calculated from this subset of the data. The elevation of the water level logger was measured with differential GPS to determine the elevation of the measured mean water level on the ellipsoid reference frame of the differential GPS data (WGS84).

In spite of this approach, several days to a week is not enough time to precisely capture seasonal or multi year signals in sea level and tides. The temperature of the water is also a major seasonal component to sea level, and in non-tropical areas this effect may be as large as 30 cm (69). In the tropical Bahamas where temperatures vary little throughout the year, this effect is likely much smaller (<10 cm).

To assess the higher frequency mean water level variability, the mean water level calculation was bootstrapped with a range of tidal cycle lengths and starting points. This bootstrap results in

a 9 cm range in the calculated mean water level for our Nassau water level data. Without a multiyear tidal record in the Bahamas, measuring the uncertainty in estimating mean water levels from short week-long datasets is not possible. However, it seems that seasonal signals should be relatively small in the region, and higher frequency variations from our recorded intervals are similar to the differential GPS uncertainty. Therefore, we assume that the uncertainty associated with measuring mean sea level with data from a small set of tidal cycles is ±10 cm.

To estimate the elevation and uncertainty of mean tide level around the archipelago, the Settlement Point long-term record, and our tidal data were combined with the EGM2008 geoid model using a 2D Gaussian process regression. In addition to the tide gauge data, the input data to the Gaussian process regression included EGM2008 geoid sampled in a 0.04 Latitude and Longitude grid. The uncertainty ascribed to the geoid data was set to the standard deviation of the residuals between the EGM2008 geoid and MSL at Settlement Point, Grand Bahama and our tide gauge stations (σ =0.76 m). The kernel used for this regression is the sum of two Matèrn covariance functions with $\nu = \frac{3}{2}$, and the variance and length scale parameters were fit to the tidal and geoid data prior to calculating the regression. Using this estimated MSL surface, each GPS measurement was adjusted to local mean sea level, and the uncertainty in that MSL estimation was added to the GPS uncertainty in quadrature. Note that the uncertainty in MSL increases away from tidal measurements.

Mapping landforms across the archipelago with neural networks. A landform map of aeolian ridges, LIG limestone flats, and Holocene marshes and strandplains was created for the Bahamian Islands and Turks and Caicos. This map is based on a combination of satellite-derived digital elevation data (TanDEM-X from the German Aerospace Center) and our own field surveys of West Caicos, San Salvador, New Providence, Great Inagua, Long Island, and Crooked Island. The TanDEM-X data was downsampled from a pixel resolution of 11 meters to 27 meters for faster computational times. This elevation data was then converted from the provided geoid reference frame (WGS84) to elevation above mean sea level by subtracting our tidal surface map (see previous section).

This elevation map was converted into a map of landforms using a convolutional neural network. Specific landforms (ridges, flats, marshes) have specific characteristic elevations and geographic patterns. A set of input data was created to teach the network how to distinguish these landforms. To create this input data, we first manually mapped landforms across the region. Ridge features were assumed to be aeolian dunes. Modern depositional systems, such as active strand plains and tidal marshes, were distinguished by eye on satellite images. The remaining land area, which was classified as limestone flats, is a mostly forested surface that tends to have abundant dissolution collapse features (sinkholes). Then, 15,000 random latitude and longitude pairs were selected from each landform class. The input data consists of a 51x51 pixel grid of elevation data centered on the latitude and longitude of each pair (pixel dimension $\sim$ 30 m). 10% of this input data was held back from the training process. This validation data offers some insight into the ability of the network to perform on data it never specifically learned from. The remaining 90% of the input data is the training data.

The training data was fed into a convolutional neural net with ten processing layers between the input and the output. First the observed training data pass through two convolutional layers that each have 32 convolutional kernels (or learned filters). The filter dimension is 3x3 pixels. Next the partially processed information flows into a 2x2 pixel downsampling layer (max pooling), after which a 25% dropout is applied. This downsampled information passes through four more layers that are similar to the first four layers with one modification: the two convolutional layers have 64 kernels each. At this point, the information is flattened into a single array and fed through a fully connected, or dense layer, that contains 512 nodes (or neurons). The activation function for each node in this layer is a rectified linear unit. After the fully connected layer, another dropout layer is applied with a 50% dropout probability. The final output layer is another fully connected layer, this time with a softmax activation function. The output layer has three nodes, one for each landform classification.

This process transforms a 51x51 pixel map of elevation data surrounding a training point into three numbers that are the probability of the input data matching each of the three landform classifications. Before training the network, all of the layer parameters and filters are initialized randomly (Glorot uniform; (70)). In this state, the ability of the network to classify the training data will be as good as randomly drawing classifications. However, by comparing predictions to the correct answer, the backward propagation of errors is used to train the network parameters to improve performance. The network was optimized using an adaptive learning rate algorithm known as *Adam* (71). After one pass through the training data (an epoch) the network performance jumps from an initial accuracy of 33% to 81% on training data. Training was terminated after 73 epochs where training accuracy was 99.7% and validation accuracy was 98.22%. This trained network was then used to convert every above sea level pixel in the TanDEM-X digital elevation dataset into a landform classification. In the end, we produce Figs. S1 and S2 which shows the elevation and distribution of the LIG flats across the entire archipelago. In the results section we relate these observations, and the variation in their elevation across the archipelago, to past sea level.

For the seven islands with outcrop surveys, the satellite-derived elevations of LIG marine flats (Fig. S5 A, grey distributions) are compared to peak sea level determined from outcrop (Fig. S5 A, white distributions). On New Providence Island (Nassau), the elevation of the highest limestone flats are very close to the outcrop estimate of peak LIG sea level, as expected. The elevation of the highest limestone flats on each of the remaining six surveyed islands is generally higher than the corresponding outcrop estimates of peak sea level by a few meters (Fig. S1). We suggest that this difference exists because the interiors of these six islands are covered in secondary growth blackland coppice forests. On the heavily populated New Providence Island, most forests have been cleared and the satellite-derived elevations more closely approximate the rocky surface. Because the other islands are forested, satellite-derived elevations represent the canopy top, and the relationship between satellite-derived elevations and LIG peak sea level for these islands should be similar to that observed on the six surveyed forested islands. The outcrop estimate of peak sea level on these six islands is equal to the 50 ±11 percentile of the distribution of limestone flat elevations (Fig. S1). When this percentile is used to estimate peak LIG sea level around the archipelago, the estimates are consistent with the field observations discussed above. In the analysis, an uncertainty of ±2 m is applied to the satellite-derived estimates to account for the differences between satellite and field observations. Even with this large uncertainty, it is clear that both data sets exhibit a significant regional pattern across the archipelago where peak LIG sea level decreases to the south and west.

GIA modeling . To calculate the gravitationally self-consistent sea level response to changes in ice and ocean load we solve the sea level equation following the algorithm by (72). This formalism allows for the migration of shorelines and takes the motion of Earth's rotation axis in response to surface load changes into account. This model requires as input viscoelastic properties of Earth's interior that are assumed to be spherically symmetric. We use the density and elastic structure from PREM (73) and vary three parameters for the viscosity structure: upper mantle viscosity, lower mantle viscosity, and elastic thickness of the lithosphere. The upper mantle is defined as the region below the lithosphere and extending to 660 km. The lower mantle extends from this depth to the core-mantle boundary. We vary the elastic thickness of the lithosphere between 71 km and 96 km, the upper mantle viscosity between 0.3 and 0.5×10^{21} Pa·s, and the lower mantle viscosity between 3 and 40×10^{21} Pa·s.

In addition to the Earth structure, GIA models also require an assumption about the temporal evolution of past ice sheets that drive the crustal/mantle deformation. We use the ICE-6G reconstruction (74) for the last deglaciation and follow the foraminifera isotope-based eustatic curve by (75) prior to the the last glacial maximum (LGM). Based on this curve, the assumed eustatic value at 128 ka is -75m, which is at odds with coral evidence from the many locations that indicate sea level must have been close to present at that time (3, 29, 76). To account for this discrepancy, we shift the eustatic curve prior to the LIG back by 3.5 ka. This shift allows for a longer interglacial time period without changing the deglaciation pattern

of the original curve and places the MIS 6 sea level lowstand at 135.5 ka. However, constraints from Tahitian corals (77) indicate that local sea level was already -85 m or higher by 137 ka and that the deglaciation had started by 142 ka. To explore the uncertainty associated with this deglacial timing, we run simulations with two ESL curves, one that has its MIS 6 maximum at 135.5ka and one that has it at 142ka (see Fig. S7). We don't include a sea level oscillation during the deglaciation as was proposed by (77) and (78). In order to investigate deviations relative to present-day sea level, we set the excess eustatic sea level during the LIG (assumed here to last from 128 ka to 117 ka) to 0 m (Fig. 1C).

We start the GIA model runs at MIS 11 (400 ky) following the shifted sea level curve by (75). To obtain ice sheet geometries from the eustatic curve prior to the LGM, we assume correspondence between ice sheet geometry and eustatic value during the last deglaciation to extrapolate back in time. This (typical) approach results in an ice sheet configuration during MIS 6 that obviously resembles the LGM (MIS 2). However, evidence exists that the Fennoscandian ice sheet was bigger (and consequently the Laurentide ice sheet likely smaller) during MIS6 (48–50). To explore this uncertainty, our GIA models were run with three ice sheet configurations: (1) a reconstruction where the MIS 6 ice sheet configuration is the same as MIS 2 (Laurentide Ice Sheet LIS=89 m sea level equivalent ice volume SLE), (2) the reconstruction of a larger Fennoscandian MIS 6 ice sheet by (48) that is constrained by deformed shorelines and ice margins (LIS=59 m SLE), and (3) a reconstruction of an even larger Fennoscandian ice sheet from (49) that is derived from coupling climate models to paleoenvironmental proxy data from MIS 6 (LIS=43 m). These are the same ice sheet configurations that were explored in (19)). We explore three additional ice distributions between scenario (1) and scenario (2) with the LIS equal to either 81, 73, or 66 m SLE. For all of the ice sheet reconstructions, we assume that the increase in ice mass in the Fennoscandian ice sheet was perfectly compensated by a decrease in ice mass over North America. The contributions from the Antarctic and Greenland ice sheet are not varied (other than for different GMSL scenarios). Their contribution is small and will not lead to significant changes investigated here. However, their melt contribution will lead to distinct patterns over the course of the LIG, which is discussed in the text. The six ice-loading histories are paired with the range of viscoelastic structures and eustatic sea level curves described above to result in a suite of GIA predictions for the Bahamas. Varying both Earth and ice history leads to 576 different GIA predictions for the Bahamian archipelago.

In addition to the suite of 1D GIA models we investigated three 3D GIA models. These models use an ice history based on a Fennoscandian MIS 6 ice sheet (48) and a slower deglaciation based on (77). The 3D viscosity structure is dervied from the seismic tomography model SL2013sv by (79, 80) above the transition zone and SEMUCB-WM1 by (81) below the transition zone. Seismic wave speed is converted into viscosity using a series of rheological relationships (82) in which conversion parameters are obtained my fitting first-order geodynamic observations (83). The boundary between the lithosphere and asthenosphere is based on the 1175°C isothermal surface and the 3D viscosity structure is imposed on a radial profile. 40×10^{21} Pa·s The three different simulations differ by their radial profile. The first simulations assumes an average lithospheric thickness of 100 km and a viscosity of 5×10^{20} Pa·s and 5×10^{21} Pa·s in the upper and lower mantle, respectively. The second simulation uses the same viscosity but assumes a thinner average lithospheric thickness of 80 km. The third simulation differs from the first by using a lower viscosity in the lower mantle (1.6×10^{21} Pa·s down to a depth of 1175 km and 3×10^{21} Pa·s below that). The 3D GIA calculation is performed using the code described in (84). More information on the viscosity structure and ice history can be found in (85).

Estimating GMSL change during the LIG . Bayesian gaussian process regression was used to estimate GMSL during the LIG from published elevations and ages of corals as well as our observations of late LIG peak sea level. Each sea level observation is corrected for the indicative water depth range of the observation, the long term subsidence of the archipelago, and for GIA using a weighted combination of 576 distinct GIA models. The gaussian process framework allows us to incorporate data with very different age uncertainties and indicative water depth ranges to estimate how GMSL (and the uncertainty) changes over time.

GMSL is assumed to be a gaussian process with a covariance function that is the sum of a radial basis function (RBF) and a white noise kernel. We set a prior distribution for the length scale for the RBF kernel to an inverse gaussian distribution with $\mu = 2$ and $\lambda = 5$. This lengthscale effectively ignores changes on short timescales (100s of years) and timescales longer than the LIG (>10 ka). A normal gaussian distribution with $\mu = 0$ and $\sigma = 5$ is used as a prior for the square root of the variance of the RBF function. A half (positive only) Student T distribution with $\nu = 1$ and $\sigma = 0.1$ is used as a prior for the variance of the white noise kernel. The peak sea level estimates from the neural network analysis are treated as sea level marine-limiting points with a uniform flat prior that forces the point underwater. The prior for the age of these sea level estimates is set to 116 ka plus an inverse gaussian distribution with $\mu = 2$ and $\lambda = 5$ (in other words, the ages are modeled as late LIG with the peak around 117 ka and an asymmetric higher tail that extends up to about 122 ka). This prior was designed to capture our geologic interpretations of the observations as described in the beginning of the results and discussion section while also agreeing with comparisons to the predicted gradients in GIA throughout the LIG. The elevations of the contact between aeolian and underlying beach facies were interpreted as the elevation of paleo-ordinary berms. This offset from mean sea level was modeled as a normal distribution where the mean ordinary berm elevation was calculated using IMCalc application (63) at each location today (μ is between 0.86 m and 1.28 m), and the uncertainty prescribed is equal to the standard deviation of berm elevations ($\sigma = 0.17m$) across the entire dataset.

The age and uncertainty of the corals is set to the reported values bounded by the start (128 ka) and end (117 ka) of the LIG in our GIA model runs (27, 29, 44, 62). The elevations of the corals are normally distributed about the reported elevation and uncertainties from (62) and (54). The water depth of each coral is modeled separately with a inverse gaussian distribution, where μ and λ are scaled so that the 95th percentile matches reported maximum water depths. This prior for the coral water depth is consistent with the water depth interpretations of these sites presented in (54) and (44). The long-term subsidence of the islands is considered to be the same across the archipelago and is modeled as a normal distribution centered at 2.5 meters with a standard deviation of 0.5 meter (the observed rate from cores on Andros Island is 2.5 m per 125 ky; (24, 47)).

Posterior distributions were sampled with the *No U-Turn Sampler (NUTS)* using the python probabilistic programming package PyMC3 (86, 87). The posterior GMSL distribution was calculated for each GIA model separately. The next section will describe how each of these statistical models are combined into a meta-model that contains our best estimate of past GMSL. The GMSL prior is a function of the priors on the covariance and variance parameters of the gaussian process regression. The prior GMSL will be flat throughout the LIG with normally distributed uncertainty (2-σ)of $\pm$10 m centered about zero (although with data this *prior* is centered about the mean of the data).

Combining GMSL estimates with Bayesian Model Averaging . Bayesian model averaging was used to determine the relative probability that a given GIA model can explain the observations. For example, a perfect or *True* GIA model would completely remove all spatial variations in the paleo sea-level data (assuming no other spatially variable processes). The statistical framework described above allows us to explicitly include uncertainties in age and sea level while determining the probability that each GIA model could generate the observations (among the 576 compared models). More specifically, we use *Pareto smoothed importance sampling* to approximate leave-one-out cross-validation (LOO) (88). The LOO cross-validation is used to generate relative weights that describe the probability of each model to have generated the data (89). These weights essentially describe the predictive power of each model (in other words how well the model performs at predicting observations that are with-held from model training.) These calculations were implemented using ArviZ (90). These weights are then used to create a meta-model that combines information learned from each model-data comparison. This meta-model can generally be thought

of as a weighted-mean. One realization of the posterior in this meta model is generated by calculating a weighted mean that combines individual posterior realizations from each of the 576 GIA models. Generally speaking, we continue to generate new realizations of this posterior until the statistics of interest stop changing significantly. In other words, when the posterior mean and variance start to converge, enough realizations have been generated.

All data, models, and code used in this work are available at https://github.com/blakedyer/bahamas_lig/.

ACKNOWLEDGMENTS. This material is based upon work supported by the National Science Foundation under Grants OCE-1202632 'PLIOMAX' and OCE-1841888. TanDEM-X digital elevation data is under copyright by the German Aerospace Center (DLR). All rights reserved, used with permission within the Project DEM_GEOL1210 (A. Rovere / M.E. Raymo). M. E. Raymo and J. Austermann gratefully acknowledge support from the Vetlesen Foundation. Alessio Rovere's research on Last Interglacial was funded by the Institutional Strategy of the University of Bremen (German Excellence Initiative, grant n. ABPZuK-03/2014) and European Research Council (ERC) under the European Unions Horizon 2020 research and innovation programme (grant agreement No. 802414). We are thankful The Bahamas Environment, Science & Technology (BEST) Commission, the Gerace Research Center on San Salvador Island, and many Bahamian people for support of our field work. This work benefited from many discussions with the 'PLIOMAX' community. The authors acknowledge PALSEA, a working group of the International Union for Quaternary Sciences (INQUA) and Past Global Changes (PAGES), which in turn received support from the Swiss Academy of Sciences and the Chinese Academy of Sciences

1. RE Kopp, FJ Simons, JX Mitrovica, AC Maloof, M Oppenheimer, Probabilistic assessment of sea level during the last interglacial stage. *Nature* **462**, 863–869 (2009).
2. A Dutton, K Lambeck, Ice volume and sea level during the last interglacial. *Science* **337**, 216–219 (2012).
3. A Dutton, et al., Sea-level rise due to polar ice-sheet mass loss during past warm periods. *Science* **349**, aaa4019 (2015).
4. NP McKay, JT Overpeck, BL Otto-Bliesner, The role of ocean thermal expansion in Last Interglacial sea level rise. *Geophys. Res. Lett.* **38** (2011).
5. A Levermann, et al., The multimillennial sea-level commitment of global warming. *Proc. Natl. Acad. Sci.* **110**, 13745–13750 (2013).
6. RM DeConto, D Pollard, Contribution of Antarctica to past and future sea-level rise. *Nature* **531**, 591–597 (2016).
7. KM Cuffey, SJ Marshall, Substantial contribution to sea-level rise during the last interglacial from the Greenland ice sheet. *Nature* **404**, 591 (2000).
8. W Farrell, JA Clark, On postglacial sea level. *Geophys. J. Int.* **46**, 647–667 (1976).
9. W Peltier, J Andrews, Glacial-Isostatic Adjustment—I. The Forward Problem. *Geophys. J. Int.* **46**, 605–646 (1976).
10. K Lambeck, M Nakada, Constraints on the age and duration of the last interglacial period and on sea-level variations. *Nature* **357**, 125 (1992).
11. CP Conrad, The solid Earth's influence on sea level. *Geol. Soc. Am. Bull.* **125**, 1027–1052 (2013).
12. WR Peltier, Ice Age Paleotopography. *Science* **265**, 195–201 (1994).
13. N Haskell, The motion of a viscous fluid under a surface load. *Physics* **6**, 265–269 (1935).
14. CL Pekeris, Thermal convection in the interior of the Earth. *Geophys. J. Int.* **3**, 343–367 (1935).
15. AM Forte, WR Peltier, The kinematics and dynamics of poloidal–toroidal coupling in mantle flow: The importance of surface plates and lateral viscosity variations. *Adv. Geophys.* **36**, 1–119 (1994).
16. R Moucha, et al., Dynamic topography and long-term sea-level variations: There is no such thing as a stable continental platform. *Earth Planet. Sci. Lett.* **271**, 101–108 (2008).
17. ME Raymo, JX Mitrovica, MJ O'Leary, RM DeConto, PJ Hearty, Departures from eustasy in Pliocene sea-level records. *Nat. Geosci.* **4**, 328 (2011).
18. J Austermann, JX Mitrovica, P Huybers, A Rovere, Detection of a dynamic topography signal in last interglacial sea-level records. *Sci. Adv.* **3**, e1700457 (2017).
19. S Dendy, J Austermann, J Creveling, J Mitrovica, Sensitivity of Last Interglacial sea-level high stands to ice sheet configuration during Marine Isotope Stage 6. *Quat. Sci. Rev.* **171**, 234–244 (2017).
20. EJ Rohling, et al., Differences between the last two glacial maxima and implications for ice-sheet, $\delta 18$O, and sea-level reconstructions. *Quat. Sci. Rev.* **176**, 1–28 (2017).
21. JX Mitrovica, Haskell [1935] revisited. *J. Geophys. Res. Solid Earth* **101**, 555–569 (1996).
22. HC Lau, et al., Inferences of mantle viscosity based on ice age data sets: Radial structure. *J. Geophys. Res. Solid Earth* **121**, 6991–7012 (2016).
23. A Rovere, et al., The Mid-Pliocene sea-level conundrum: Glacial isostasy, eustasy and dynamic topography. *Earth Planet. Sci. Lett.* **387**, 27–33 (2014).
24. DF McNeill, Accumulation rates from well-dated late Neogene carbonate platforms and margins. *Sedimentary Geol.* **175**, 73–87 (2005).
25. P Garrett, SJ Gould, Geology of New Providence Island, Bahamas. *Geol. Soc. Am. Bull.* **95**, 209–220 (1984).
26. B White, KA Kurkjy, HA Curran, KA Besom, Shallowing-Upward Sequence in a Pleistocene Coral Reef and Associated Facies, San Salvador, Bahamas. *AAPG Bull.* **68**, 539–539 (1984).
27. J Chen, H Curran, B White, G Wasserburg, Precise chronology of the last interglacial period: 234U-230\textsuperscriptTh data from fossil coral reefs in the Bahamas. *Geol. Soc. Am. Bull.* **103**, 82–97 (1991).
28. JL Carew, JE Mylroie, Quaternary tectonic stability of the Bahamian Archipelago: Evidence from fossil coral reefs and flank margin caves. *Quat. Sci. Rev.* **14**, 145–153 (1995).
29. WG Thompson, HA Curran, MA Wilson, B White, Sea-level oscillations during the last interglacial highstand recorded by Bahamas corals. *Nat. Geosci.* **4**, 684–687 (2011).
30. LV Illing, Bahaman calcareous sands. *AAPG bulletin* **38**, 1–95 (1954).
31. M Ball, Carbonate sand bodies of Florida and the Bahamas. *J. Sedimentary Res.* **37**, 556–591 (1967).
32. PJ Hearty, AC Neumann, DS Kaufman, Chevron ridges and runup deposits in the Bahamas from storms late in oxygen-isotope substage 5e. *Quat. Res.* **50**, 309–322 (1998).
33. P Kindler, A Strasser, Palaeoclimatic significance of co-occurring wind-and water-induced sedimentary structures in the last-interglacial coastal deposits from Bermuda and the Bahamas. *Sedimentary Geol.* **131**, 1–7 (2000).
34. J Bourgeois, R Weiss, "Chevrons" are not mega-tsunami deposits—A sedimentologic assessment. *Geology* **37**, 403–406 (2009).
35. L Vimpere, P Kindler, S Castelltort, Chevrons: Origin and relevance for the reconstruction of past wind regimes. *Earth-Science Rev.* (2019).
36. DE Hattin, VL Warren, Stratigraphic analysis of a fossil Neogoniolithon-capped patch reef and associated facies, San Salvador, Bahamas. *Coral Reefs* **8**, 19–30 (1989).
37. C Kerans, C Zahm, SL Bachtel, P Hearty, H Cheng, Anatomy of a late Quaternary carbonate island: Constraints on timing and magnitude of sea-level fluctuations, West Caicos, Turks and Caicos Islands, BWI. *Quat. Sci. Rev.* **205**, 193–223 (2019).
38. T Tamura, Beach ridges and prograded beach deposits as palaeoenvironment records. *Earth-Science Rev.* **114**, 279–297 (2012).
39. A Strasser, E Davaud, Formation of Holocene limestone sequences by progradation, cementation, and erosion; two examples from the Bahamas. *J. Sedimentary Res.* **56**, 422–428 (1986).
40. EK Potter, K Lambeck, Reconciliation of sea-level observations in the Western North Atlantic during the last glacial cycle. *Earth Planet. Sci. Lett.* **217**, 171–181 (2004).
41. GA Milne, M Peros, Data–model comparison of Holocene sea-level change in the circum-Caribbean region. *Glob. Planet. Chang.* **107**, 119–131 (2013).
42. R Love, et al., The contribution of glacial isostatic adjustment to projections of sea-level change along the Atlantic and Gulf coasts of North America. *Earth's Futur.* **4**, 440–464 (2016).
43. NS Khan, et al., Drivers of Holocene sea-level change in the Caribbean. *Quat. Sci. Rev.* **155**, 13–36 (2017).
44. DR Muhs, KR Simmons, RR Schumann, ES Schweig, MP Rowe, Testing glacial isostatic adjustment models of last-interglacial sea level history in the Bahamas and Bermuda. *Quat. Sci. Rev.* **233**, 106212 (2020).
45. AC Neumann, PJ Hearty, Rapid sea-level changes at the close of the last interglacial (substage 5e) recorded in Bahamian island geology. *Geology* **24**, 775–778 (1996).
46. PJ Hearty, AC Neumann, Rapid sea level and climate change at the close of the Last Interglaciation (MIS 5e): Evidence from the Bahama Islands. *Quat. Sci. Rev.* **20**, 1881–1895 (2001).
47. GW Lynts, Conceptual model of the Bahamian Platform for the last 135 million years. *Nature* **225**, 1226 (1970).
48. K Lambeck, et al., Constraints on the Late Saalian to early Middle Weichselian ice sheet of Eurasia from field data and rebound modelling. *Boreas* **35**, 539–575 (2006).
49. F Colleoni, C Wekerle, JO Näslund, J Brandefelt, S Masina, Constraint on the penultimate glacial maximum Northern Hemisphere ice topography $(\approx 140$ kyrs BP). *Quat. Sci. Rev.* **137**, 97–112 (2016).
50. CL Batchelor, et al., The configuration of Northern Hemisphere ice sheets through the Quaternary. *Nat. Commun.* **10**, 1–10 (2019).
51. NLM Barlow, et al., Lack of evidence for a substantial sea-level fluctuation within the Last Interglacial. *Nat. Geosci.* **11**, 627–634 (2018).
52. B White, HA Curran, MA Wilson, Bahamian coral reefs yield evidence of a brief sea-level lowstand during the last interglacial. *Carbonates Evaporites* **13**, 10 (1998).
53. MA Wilson, HA Curran, B White, Paleontological evidence of a brief global sea-level event during the last interglacial. *Lethaia* **31**, 241–250 (1998).
54. A Skrivanek, J Li, A Dutton, Relative sea-level change during the Last Interglacial as recorded in Bahamian fossil reefs. *Quat. Sci. Rev.* **200**, 160–177 (2018).
55. C Hay, et al., The sea-level fingerprints of ice-sheet collapse during interglacial periods. *Quat. Sci. Rev.* **87**, 60–69 (2014).
56. J Jouzel, et al., Orbital and millennial Antarctic climate variability over the past 800,000 years. *science* **317**, 793–796 (2007).
57. D Dahl-Jensen, et al., Eemian interglacial reconstructed from a Greenland folded ice core. *Nature* **493**, 489 (2013).
58. M Helsen, W Van De Berg, R Van De Wal, M Van Den Broeke, J Oerlemans, Coupled regional climate–ice-sheet simulation shows limited Greenland ice loss during the Eemian. *Clim. Past* **9**, 1773–1788 (2013).
59. AM Yau, ML Bender, A Robinson, EJ Brook, Reconstructing the last interglacial at Summit, Greenland: Insights from GISP2. *Proc. Natl. Acad. Sci.* **113**, 9710–9715 (2016).
60. JL Bamber, RE Riva, BL Vermeersen, AM LeBrocq, Reassessment of the potential sea-level rise from a collapse of the West Antarctic Ice Sheet. *science* **324**, 901–903 (2009).
61. D Farinotti, et al., A consensus estimate for the ice thickness distribution of all glaciers on Earth. *Nat. Geosci.* **12**, 168–173 (2019).
62. FD Hibbert, et al., Coral indicators of past sea-level change: A global repository of U-series dated benchmarks. *Quat. Sci. Rev.* **145**, 1–56 (2016).
63. T Lorscheid, A Rovere, The indicative meaning calculator – quantification of paleo sea-level relationships by using global wave and tide datasets. *Open Geospatial Data, Softw. Standards* **4**, 10 (2019).
64. VJ Polyak, et al., A highly resolved record of relative sea level in the western Mediterranean

Sea during the last interglacial period. *Nat. Geosci.* **11**, 860–864 (2018).
65. PU Clark, et al., Oceanic forcing of penultimate deglacial and last interglacial sea-level rise. *Nature* **577**, 660–664 (2020).
66. M Aurell, DF McNeill, T Guyomard, P Kindler, Pleistocene shallowing-upward sequences in New Providence, Bahamas; signature of high-frequency sea-level fluctuations in shallow carbonate platforms. *J. Sedimentary Res.* **65**, 170–182 (1995).
67. B White, HA Curran, Coral reef to eolianite transition in the Pleistocene rocks of Great Inagua, Bahamas. (1987).
68. P Caldwell, M Merrifield, P Thompson, Sea level measured by tide gauges from global oceans–the Joint Archive for Sea Level holdings (NCEI Accession 0019568), Version 5.5, NOAA National Centers for Environmental Information, Dataset. *Centers Environ. Information, Dataset* **10**, V5V40S7W (2015).
69. BC Douglas, Sea level change in the era of the recording tide gauge in *International Geophysics*. (Elsevier) Vol. 75, pp. 37–64 (2001).
70. X Glorot, Y Bengio, Understanding the difficulty of training deep feedforward neural networks in *Proceedings of the Thirteenth International Conference on Artificial Intelligence and Statistics*. pp. 249–256 (2010).
71. DP Kingma, J Ba, Adam: A method for stochastic optimization. *arXiv preprint arXiv:1412.6980* (2014).
72. RA Kendall, JX Mitrovica, GA Milne, On post-glacial sea level–II. Numerical formulation and comparative results on spherically symmetric models. *Geophys. J. Int.* **161**, 679–706 (2005).
73. AM Dziewonski, DL Anderson, Preliminary reference Earth model. *Phys. earth planetary interiors* **25**, 297–356 (1981).
74. W Peltier, D Argus, R Drummond, Space geodesy constrains ice age terminal deglaciation: The global ICE-6G_C (VM5a) model. *J. Geophys. Res. Solid Earth* **120**, 450–487 (2015).
75. C Waelbroeck, et al., Sea-level and deep water temperature changes derived from benthic foraminifera isotopic records. *Quat. Sci. Rev.* **21**, 295–305 (2002).
76. P Blanchon, A Eisenhauer, J Fietzke, V Liebetrau, Rapid sea-level rise and reef backstepping at the close of the last interglacial highstand. *Nature* **458**, 881 (2009).
77. AL Thomas, et al., Penultimate deglacial sea-level timing from uranium/thorium dating of Tahitian corals. *Science* **324**, 1186–1189 (2009).
78. M Siddall, E Bard, EJ Rohling, C Hemleben, Sea-level reversal during Termination II. *Geology* **34**, 817–820 (2006).
79. AJ Schaeffer, S Lebedev, Global shear speed structure of the upper mantle and transition zone. *Geophys. J. Int.* **194**, 417–449 (2013).
80. A Schaeffer, S Lebedev, Imaging the North American continent using waveform inversion of global and USArray data. *Earth Planet. Sci. Lett.* **402**, 26–41 (2014).
81. SW French, BA Romanowicz, Whole-mantle radially anisotropic shear velocity structure from spectral-element waveform tomography. *Geophys. J. Int.* **199**, 1303–1327 (2014).
82. H Yamauchi, Y Takei, Polycrystal anelasticity at near-solidus temperatures. *J. Geophys. Res. Solid Earth* **121**, 7790–7820 (2016).
83. FD Richards, MJ Hoggard, N White, S Ghelichkhan, Quantifying the Relationship Between Short-Wavelength Dynamic Topography and Thermomechanical Structure of the Upper Mantle Using Calibrated Parameterization of Anelasticity. *J. Geophys. Res. Solid Earth* **125** (2020).
84. K Latychev, et al., Glacial isostatic adjustment on 3-D Earth models: A finite-volume formulation. *Geophys. J. Int.* **161**, 421–444 (2005).
85. J Austermann, MJ Hoggard, K Latychev, JX Mitrovica, FD Richards, The effect of lateral variations in Earth structure on last interglacial sea level. *Geophys. J. Int.* **In review** (2021).
86. MD Hoffman, A Gelman, The No-U-Turn sampler: Adaptively setting path lengths in Hamiltonian Monte Carlo. *J. Mach. Learn. Res.* **15**, 1593–1623 (2014).
87. J Salvatier, TV Wiecki, C Fonnesbeck, Probabilistic programming in Python using PyMC3. *PeerJ Comput. Sci.* **2**, e55 (2016).
88. A Vehtari, A Gelman, J Gabry, Practical Bayesian model evaluation using leave-one-out cross-validation and WAIC. *Stat. computing* **27**, 1413–1432 (2017).
89. Y Yao, A Vehtari, D Simpson, A Gelman, Using stacking to average Bayesian predictive distributions (with discussion). *Bayesian Analysis* **13**, 917–1007 (2018).
90. R Kumar, C Carroll, A Hartikainen, OA Martín, ArviZ a unified library for exploratory analysis of Bayesian models in Python. (2019).